Role of convective parameterization in simulations of a convection band at grey-zone resolutions

Xing Yu & Tae-Young Lee

Role of convective parameterization in simulations of a convection band at grey-zone resolutions

By X I N G Y U * AND T A E - Y O U N G LEE, *Laboratory for Atmospheric Modeling Research, Department of Atmospheric Sciences, Yonsei University, Seodaemoon-ku, 120-749 Seoul, Korea*

ABSTRACT

In this study, we investigate the role of convective parameterization (CP) in simulations of a convection band over the mid-Korean Peninsula at grey-zone resolutions, at which convection is partially resolved, partially subgrid. An approach similar to that used in 'observing system simulation experiment' is adopted. Simulations with a 500-m grid size serve as benchmark simulations. The impacts of resolution and convective parameterization at grey-zone resolutions (i.e. 3, 6 and 9 km) are then investigated. Results indicate that a grid size of 3 km is sufficient to resolve the convection band and CP for this size grid is not necessary. With 6 and 9 km grids, explicit simulations or those based on a Kain–Fritsch CP scheme do not simulate the atmospheric structure surrounding the band accurately.

A major problem with CP is excessive triggering of parameterized convection. False triggers of CP in the band adjacent area suppress evolution of the resolved convection band through excessive stabilization of inflow air. We obtain significant improvements by using a modified trigger function, resulting in reduction of the area of parameterized convection, which in turn leads to stronger development of a resolved convection band. Furthermore, our approach reduces bias in the domain-averaged vertical thermodynamic structure.

1. Introduction

Current numerical weather predictions (NWPs) use high-resolution models with horizontal grid sizes of 1–10 km (Saito et al., 2007; Lean et al., 2008; Roberts and Lean, 2008). For such fine-resolution models, however, further refinements of both numerical techniques and physical parameterizations are required (Steppeler et al., 2003). One of the major problems from a physics perspective is the treatment of deep moist convection. Use of convective parameterization (CP) at fine-scale resolutions may violate underlying assumptions and the closure hypotheses upon which CP is based (Arakawa and Chen, 1987; Molinari and Dudek, 1992; Hammarstrand, 1998). For example, classical mass flux schemes assume that there is no net mass transport in the convective grid column. This assumption is not valid for NWP models with a horizontal grid size of a few kilometres. Moreover, most CP postulates a grid size large enough to cover an area that includes a statistical ensemble of convective clouds in different stages of their life cycle, because CP cannot predict the life cycle of cumulus clouds (Hammarstrand, 1998). In a high-resolution grid, an active convection cloud may move out of the grid box before it completes its life cycle.

*Corresponding author.
e-mail: yuxing@yonsei.ac.kr

It has been debated whether CP is necessary for numerical predictions of convective weather at high resolutions, where deep convection is partly resolved and partly subgrid. Gerard (2007) used the term 'grey-zone resolution' to refer to this type of resolution. Some studies suggest that a grid size smaller than 1 km is necessary to explicitly predict convective systems (Petch et al., 2002; Bryan et al., 2003; Craig and Dörnbrack, 2008). In other studies, larger grid sizes are considered sufficient for explicit simulations of mesoscale weather (e.g. 4 km in Weisman et al., 1997). Kain et al. (2008) and Schwartz et al. (2009) demonstrate that decreasing horizontal grid spacing from 4 to 2 km provides little added value considering the 10-fold increase in computational cost. In contrast, Deng and Stauffer (2006) show that grid-point storm problems can be greatly reduced by applying CP to simulations with a 4-km grid. Use of CP in the Japan Meteorological Agency's operational mesoscale NWP with a 5-km grid was found to improve the precipitation forecast (Saito et al., 2007). Use of CP is also recommended for higher resolution simulations (e.g. a 2-km grid for a simulation of a thunderstorm in a Greek case; Kotroni and Lagouvardos, 2004). Niemelä and Fortelius (2005) report that simulations of a Finland widespread convective precipitation case without CP using a grid size of 2.8-km grid yield less accurate results than those obtained using full physics by introducing a resolution-dependent CP trigger. It may be true to say that even a 1-km grid model cannot properly reproduce some convective processes such as

vertical transport, entrainment and detrainment processes in evolving cumulus clouds (Craig and Dörnbrack, 2008).

Arakawa (2004) recommended a unified cloud parameterization model in which many processes are fully coupled. Correspondingly, Gerard and Geleyn (2005) and Gerard (2007) developed a package including deep convection, resolved condensation and microphysics to solve the problem of combining resolved grids and subgrid condensation at all resolutions. This package can be used for resolutions from 2 to 100 km. It was shown that the behaviours of their scheme at grey-zone resolutions were consistent with those at lower and higher resolutions. Kuell et al. (2007) presented a hybrid approach in which only updraft and downdraft were parameterized with a net mass transport, while the subsidence in the environment was treated by grid-scale equations. They stated that this approach 'may fill the gap between coarse-grid models (grid spacing >50 km) with classical parameterization schemes and very highly resolved convection modelling (with a grid spacing of the order of 100 m)'.

Despite many extensive studies concerning the treatment of deep convections for high-resolution models, numerical simulation at grey-zone resolution is still an unsolved problem. And it is not clear yet whether CP should be used for such resolution and what grid size can be a critical value, below which CP is not necessary. In this study, we carry out an investigation to determine the role of CP in numerical simulations of a convection band at grey-zone resolutions. The Fifth-Generation Pennsylvania State University/National Center for Atmospheric Research (PSU/NCAR) Mesoscale Model (MM5) version 3.7.0 (Dudhia, 1993; Grell et al., 1994) is used. We adopt an approach similar to 'observing system simulation experiment (OSSE)'. This approach consists of three steps: (1) obtain a 'simulated true atmosphere (STA)' using a very high-resolution simulation, (2) obtain initial and boundary conditions from the STA fields for use in simulations at grey-zone resolutions (i.e. 3, 6 and 9 km grids) and (3) perform the simulations and compare them with the STA fields. For the simulation, we select the intense quasi-stationary convection band that occurred on 5–6 August 1998 over the mid-Korean Peninsula. For CP, the Kain–Fritsch Eta scheme (Kain and Fritsch, 1990, 1993; Kain, 2004) (the KF2 option in MM5) is used for parameterized convection.

In this paper, we describe the role of CP focusing on the following three aspects: (1) the dynamic and thermodynamic impacts of parameterized convection on the simulation of the convection band and its associated mesoscale circulation, (2) the resolution dependency of such impacts and (3) whether CP is necessary for simulations at grey-zone resolutions. This paper is organized as follows. Section 2 describes the methods used in this study. Section 3 presents the results of (1) the STA simulation (i.e. cloud-resolving benchmark simulation), (2) a series of simulations of the convection band at grey-zone resolutions and (3) impact analyses. In Section 4, results obtained using a modified trigger scheme in the KF CP scheme are analysed and

we discuss whether CP can improve the simulations. A summary of the results is provided in Section 5.

2. Methods

For this study, we perform an OSSE to determine the role of CP and its dependence on the horizontal grid size. The experimental procedure is described later.

2.1. Experimental design

The present experiment consists of three steps. The first step is to obtain the STA fields. This does not have to be the same as the actual atmosphere, but needs to be sufficiently representative of the real atmosphere. In this study, we obtain the STA fields using a simulation with 500-m horizontal grid spacing. Although Bryan et al. (2003) argue that finer grid resolution, for example 100-m, may be desirable for convective storm simulation, simulations with a 500-m grid can also provide realistic perspectives of deep moist convection (Adlerman and Droegemeier, 2002; Noda and Niino, 2003).

The second step is to obtain initial and boundary conditions (ICs and BCs) for simulations at grey-zone resolutions (i.e. 3-, 6- and 9-km grids) from the STA fields. The third step is to carry out the grey-zone simulations. This step consists of three groups of simulations: simulations with (1) no CP (NOCPs), (2) Kain–Fritsch CP (KFEXs) and (3) Kain–Fritsch CP with the modified trigger function of Ma and Tan (2009) (MTEXs). Each group contains three simulations with 3-, 6- and 9-km grids. For example, NOCP3, NOCP6 and NOCP9 represent the no-CP simulations with grid sizes of 3, 6 and 9 km, respectively.

The STA fields in the first step are obtained as follows. First, we conduct a simulation with two-way nesting of 27–9–3 km grids (Fig. 1). All domains (DM1, DM2 and DM3) have 23 sigma vertical levels and the model top is set to be 50 hPa. Initial fields for this simulation are from the National Centers for Environmental Prediction and National Center for Environmental Research (NCEP-NCAR) reanalysis data (Kalnay et al., 1996), with a 2.5° × 2.5° resolution at 6-h intervals from 00 UTC to 18 UTC 5 August. Surface (6 hourly) and upper-air (12 hourly) observations from the South China Sea Monsoon Experiments (SCSMEX, see Lau et al., 2000) are also considered using a successive correction scheme on the basis of first guess. No pre-forecast spin-up or assimilation of additional observations is used.

After the above-mentioned simulation is complete, an additional simulation (STA simulation) is performed to obtain the STA fields. The domain for the STA simulation is located within DM3 (the domain for the 3-km grid simulation) (Fig. 1) and contains 577 × 505 grid points with a 500-m grid size in the x and y directions. Vertically, it has 46 sigma levels (twice the number for DM3). The STA simulation starts at 06 UTC 5 August 1998 and lasts for 12 h. The ICs and BCs are interpolated
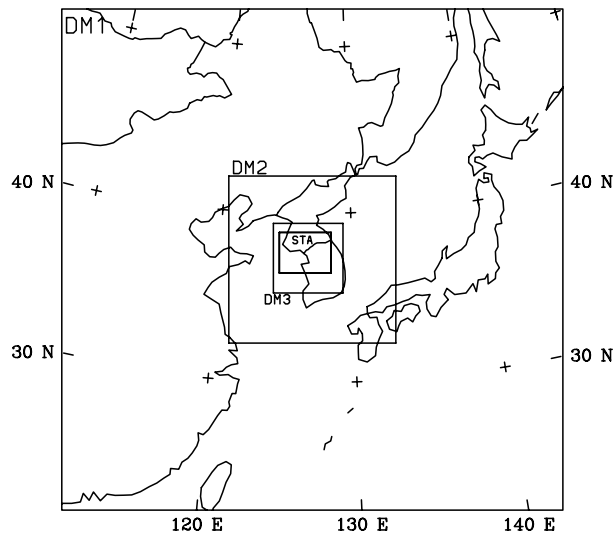
Fig. 1. Experimental domain. The smallest rectangle is the domain for the simulated true atmosphere with a 500-m horizontal grid spacing.

from the results of the 3-km grid simulation, which are stored every 10 min. The land surface is assumed to be flat to avoid inconsistencies between the model sigma level and the pressure level, given that topography is much steeper at fine resolutions. Sun and Lee (2002) showed that the Korean topography is not an essential factor for the formation of the convection band considered in this study. For consistency, the same physics package is used for both the DM3 and STA domains, except that a new horizontal diffusion scheme developed by Liu et al. (2006) is used for the STA simulation.

All the simulations in the third steps (i.e. NOCPs, KFEXs and MTEXs) are carried out in the same domain as that located within the STA domain. There are 94, 48 and 32 grids in the east-west direction and 82, 42 and 28 grids in the north-south direction for the 3-, 6- and 9-km grid models, respectively. The ICs and BCs for these simulations are calculated by averaging the STA fields. All simulations are performed for the 9-h period from 09 to 18 UTC 5 August 1998, during which the convection band forms and develops. The model physics employed for grey-zone simulations include the mixed-physics microphysics scheme of Reisner et al. (1998), Blackadar's high-resolution planetary boundary layer scheme (Zhang and Anthes, 1982) and the cloud atmospheric radiation scheme (Dudhia, 1993).

2.2. *Case*

This study considers a long-lived, quasi-stationary convection band that occurred on 5–6 August 1998 over the middle of the Korean peninsula (Figs 2 and 3). A GMS-enhanced infrared image for 15 UTC 5 August (Fig. 2) shows an extended convective system over the mid peninsula. The western part of the system extends southwestward to the sea from the coast. Sun and Lee (2002) studied this case and found that the band developed in an area of large-scale convergent flow between a mid-latitude cyclone to the north of the Korean peninsula and the western pacific subtropical high (WPSH) to the south. Low-level south-westerly flow along the northwestern rim of WPSH continuously transports warm and moist air to the area of the convection band, and this is essential for the development of the long-lived quasi-stationary convection band. This convection band at its mature stage consists of several long-lived precipitation cells along the band. It is 20- to 30-km wide and about 300-km long.

Radar images show the formation and development of this convection band in more detail (Fig. 3). A short and narrow line of weak echo develops over the coastal area at 11 UTC 5 August. The convection band develops rapidly both seaward
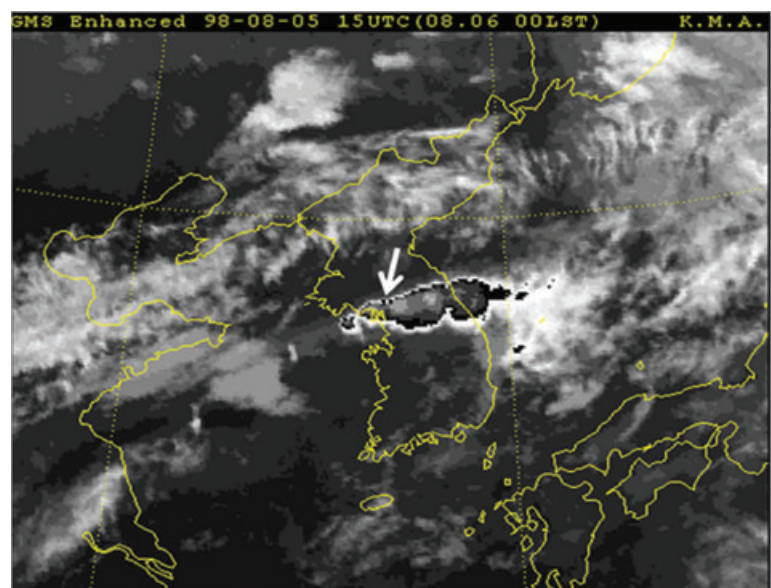

Fig. 2. GMS-enhanced IR image showing the convection band (indicated by a white arrow) over the Korean Peninsula at 15 UTC 5 August 1998.
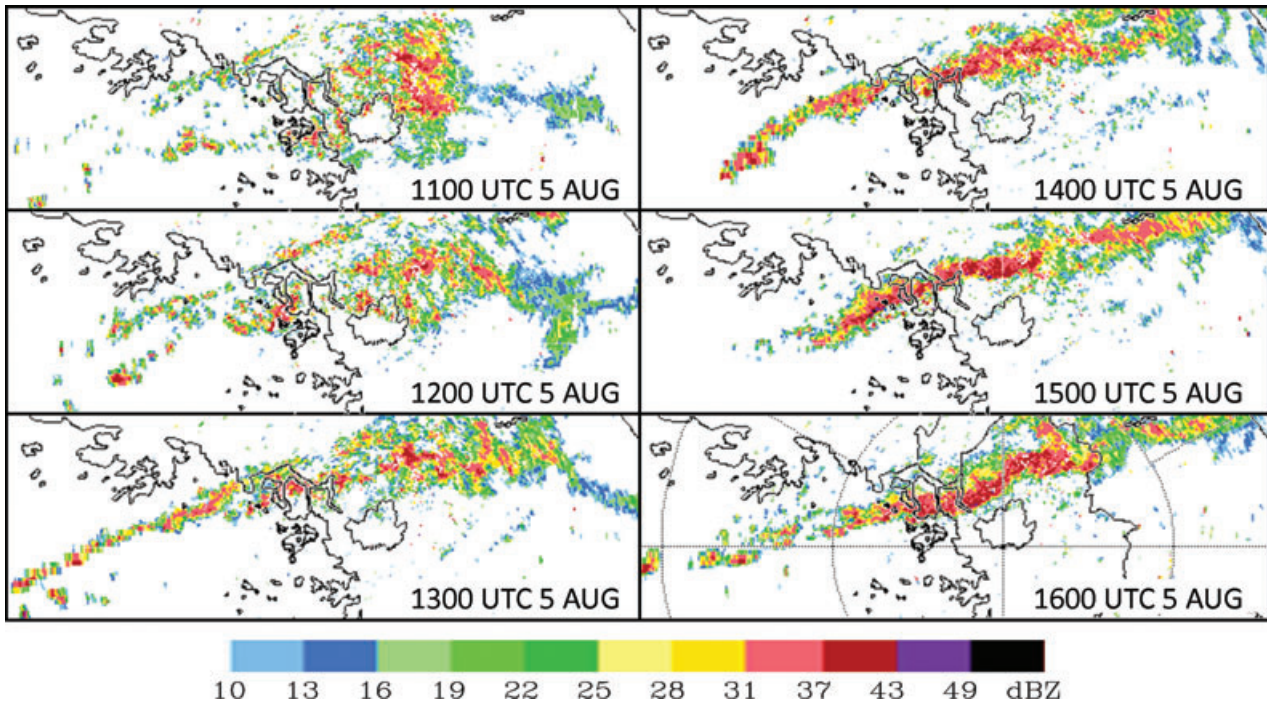
Fig. 3. Radar images showing the distribution of reflectivity associated with the convection band for the period of 1100–1600 UTC 5 August 1998. The circles in the image for 1600 UTC are the radius ranges of 100 and 200 km (from Sun and Lee, 2002).
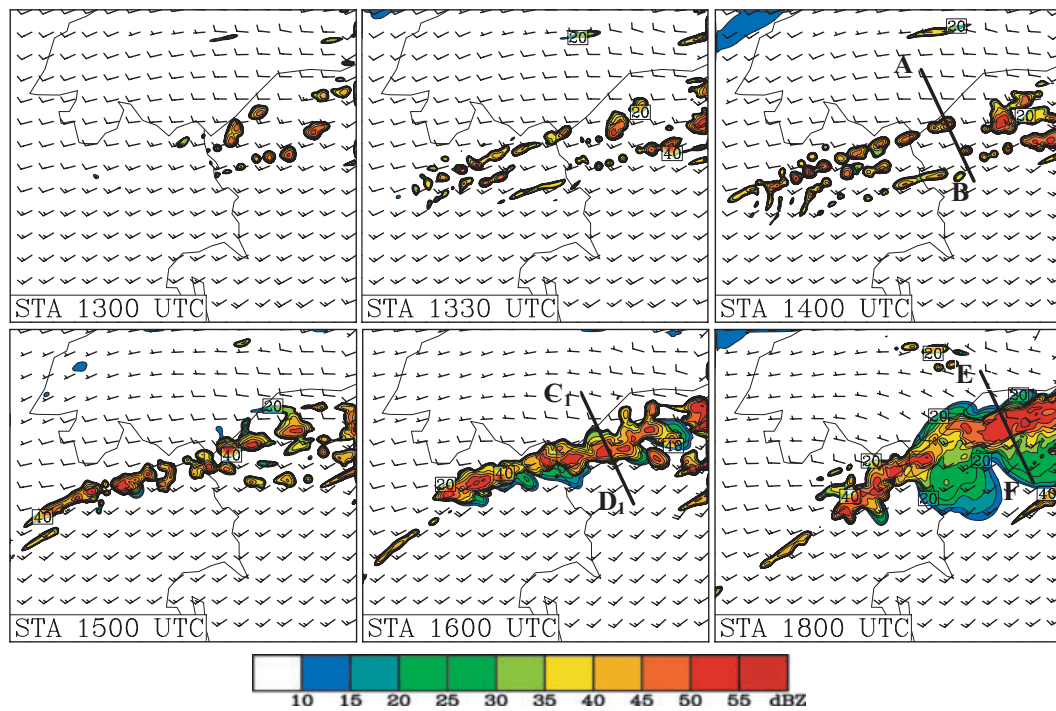

Fig. 4. Simulated wind fields at 925 hPa (the full barb represents 10 m s^{-1}) and vertical maximum radar reflectivity (dBZ) for the STA. The lines marked by 'AB' (1400 UTC), 'C$_1$D$_1$' (1600 UTC) and 'EF' (1800 UTC) indicate the locations of cross-sections shown in Fig. 5 for the three stages of band development (formation, development and mature stages, respectively).

and landward. The intensity of the echo along the line is weak during this formation stage. A well-defined echo line is present at 13 UTC. Generally, the radar echo shows a continuous line structure, although several strong cells are visible along the line. After 13 UTC, both the strength and width of the band develop further, resulting in heavy rainfalls along the band. A detailed description of this case can be found in Sun and Lee (2002).

3. Results

The STA simulation reproduces the initiation and evolution of the convective band that occurred on 5 August 1998 fairly well. In this section, we first describe the STA simulation. We then investigate the effects of CP on the simulations of the convection band at grey-zone resolutions by comparing the simulation results with the STA fields.

3.1. Simulated true atmosphere

A basic assumption of our approach is that the STA represents the real atmosphere. Here, STA fields are compared with observations. For convenience, we show the convection band using the maximum column reflectivity derived from model variables, following Weisman et al. (2008). The equivalent radar reflectivity [Ze(dBZ)] is converted from model-calculated hydrometer density values including cloud water, rain water, snow and ice as described by Thompson et al. (2004). The simulated maximum column reflectivity and horizontal flow at 925 hPa are shown in Fig. 4. Southwesterly wind dominates the southern part of the domain during all stages. At 1300 UTC, two small cells form just off the west coast. During the next 30 min, a band of convective cells, including the two small cells, develops rapidly over the sea. Landward movement of convective cells (in an ENE direction) and continued formation of cells in the upstream area of the band result in a well-defined convection band after 1330 UTC. Another short band exists to the south of the main band. The width and strength of the main band develop further and the band shows a continuous line of heavy rainfall after 1500 UTC. At its mature stage (after 1600 UTC), the band with strong echo is about 300-km long and 20- to 30-km wide. The relatively weak echo in the wide area to the south of the strong echo band is associated with anvil clouds (Fig. 5c). Continued development of a narrow convection band is seen over the sea in the upstream area.

The formation process can be summarized as the following: (1) the band is initiated from the convection cells over the coastal area; (2) it develops both seaward and landward showing more rapid development over the sea and (3) it moves eastward as embedded cells move in an ENE direction. These findings are consistent with those of Sun and Lee (2002).

To further analyse the STA fields, we divide band development into three stages: the formation stage (1200–1400 UTC), the development stage (1400–1600 UTC) and the mature stage
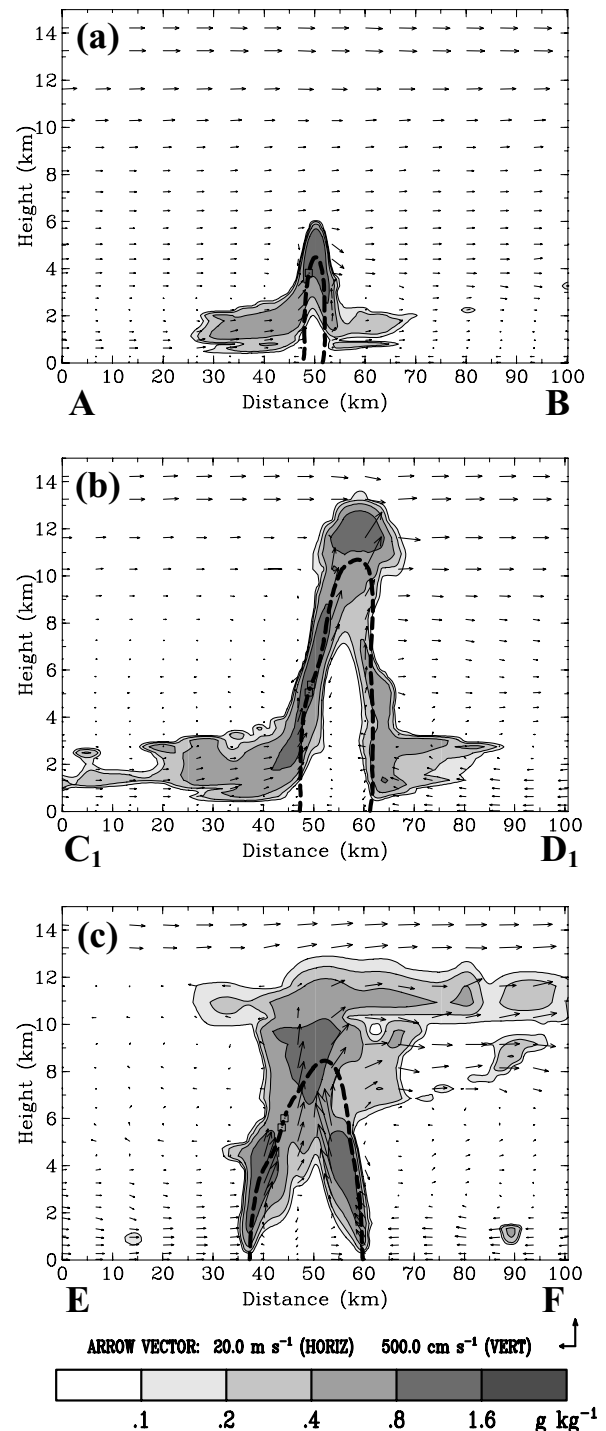

Fig. 5. Vertical cross-sections of convective system in terms of the mixing ratio of total cloud (water and ice) and air motion along the lines shown in Fig. 4: (a) 'AB', (b) 'C₁D₁' and (c) 'EF'. The shadings represent regions where the total cloud water–ice mixing ratios are 0.1, 0.2, 0.4, 0.8 and 1.6 g kg^{-1}. The thick dashed line represents the 45-dBZ contour line of simulated radar reflectivity. The wind vector is composed of horizontal wind (parallel to the cross-section) and vertical velocity. Length of wind vector scale represents 20 m s^{-1} for horizontal velocity and 5 m s^{-1} for vertical velocity, respectively.

(1600–1800 UTC). Cross-sections across the band (or convective cell) at the culmination of these three stages (1400, 1600 and 1800 UTC) are shown in Fig. 5. At 1400 UTC, the convective cell is still at a growing stage with its top reaching the 6-km level. Updrafts are found at low levels on both (northern and southern) sides of the cell and merge into one as air ascends above the middle of the cloud. Strong reflectivity (>45 dBZ) is present at the centre of the cell from the upper part to the ground level. The convective system embedded in the band at 1600 UTC has grown to the maximum height of 13 km. Its basic structure is similar to that seen for 1400 UTC, with strong updrafts up to 7 km in height on both sides of the band and merging of the updrafts at the upper part of the clouds. Strong reflectivity is found throughout the system vertically, and downdrafts are found in the section of strong reflectivity. At 1800 UTC, the convection band is at a mature stage with anvil clouds present

to the southern side of the band. Although the basic structure of the convection system is similar to that for 1600 UTC, the circulation associated with the convective system has become better defined and stronger. Updrafts at low levels are strong and they merge at a height of 4 km. Downdrafts at low levels are also strong, and form well-defined gust fronts resulting in strong lifting of air on both sides of the band. Heavy rainfall occurs along the band.

The STA simulation does not consider topography and may show significant discrepancies from the real atmosphere. However, the simulated convection band forms and develops in a manner close to that observed. We therefore assume that the simulated atmosphere (i.e. the STA simulation) represents the true atmosphere, and use the STA to obtain ICs and BCs for simulations at grey-zone resolutions (i.e. NOCPs, KFEXs and MTEXs). We also use the STA as the reference atmosphere
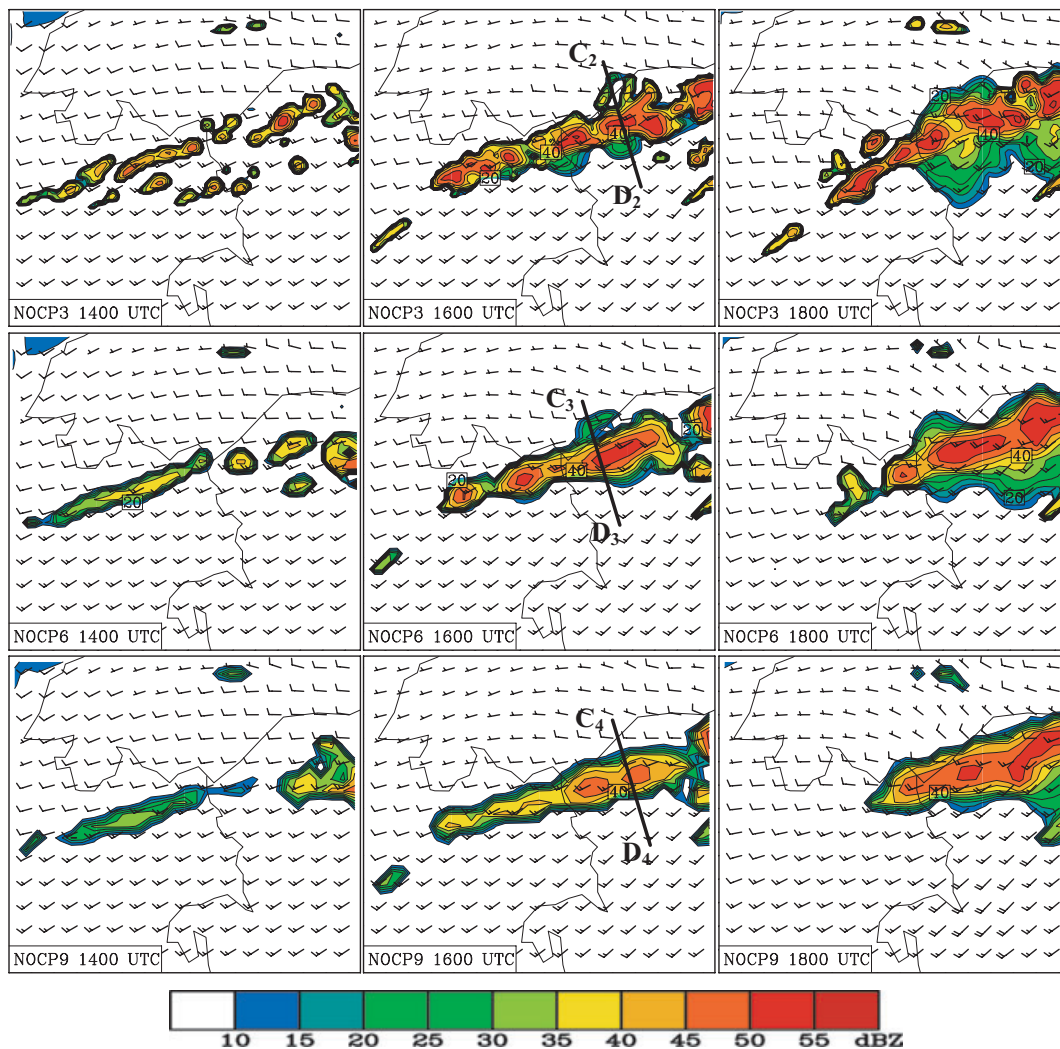

Fig. 6. Simulated vertical maximum radar reflectivity for NOCPs at 1400, 1600 and 1800 UTC. The three lines 'C$_2$D$_2$', 'C$_3$D$_3$' and 'C$_4$D$_4$' indicate the locations of cross-sections shown in Fig. 7 for NOCP3, NOCP6 and NOCP9, respectively.

against which the results of the grey-zone experiments are compared to extract the role of parameterized convection in such simulations.

3.2. Simulations without parameterized convection (NOCPs)

In this section, we analyse simulations without convective parameterization (NOCPs) to determine if they can reproduce the STA fields and to determine their dependence on grid size. We then examine the bias in the simulated environment due to neglect of CP.

The simulated maximum reflectivity fields at three stages are illustrated in Fig. 6. The fields from NOCP3 are close to those of the STA. The convection band consists of several individual cells during the development stage. NOCP6 and NOCP9 can also reproduce the convection band, although they produce fewer small-scale details than NOCP3, and band formation is delayed. In NOCP6, the band formation process is roughly similar to that for the STA, but the initial cells are weaker and form about 30 min later than for the STA (not shown). In NOCP9, a well-defined convection band forms at 1400 UTC, even though initial convective cells do not form in advance. The simulated band tends to show a continuous echo structure as grid size increases, in contrast to observations (cell-type structure). This result is expected, because a grid size larger than 6 km cannot resolve most individual cells.

Figure 7 shows the cross-sections of the convection band for 1600 UTC, the locations of which are marked in Fig. 6. The vertical structure of the band in the NOCP experiment varies with grid size. The band in NOCP3 shows a fully developed convective system with anvil clouds with a maximum height near the 13-km level. The structure of the convection system is similar to that of the STA at 1600 and 1800 UTC, showing updrafts on both sides of the band and merging of the updrafts at a level of 4 km. Downdrafts are also evident below the convective clouds. This structure becomes less clear and the depth of updraft decreases as grid size increases. Reflectivity also weakens as grid size increases. In NOCP9, the cloud top is below a height of 8 km and anvil clouds do not develop even at 1800 UTC (not shown). As seen in NOCP3, a strong outflow at the top of the convection band detrains the cloud ice to the southern side of the band. Figure 7 also indicates that simulations with 6- and 9-km grids cannot reproduce the low-level downdrafts that contribute to strong lifting of low-level air as observed in the STA. Horizontal distribution of the simulated 6-h (1200–1800 UTC) rainfall amount (Fig. 8) shows that NOCPs reproduce the narrow and intense precipitation band fairly well, except that the amount of rainfall along the band centre in NOCP9 is significantly smaller than that for NOCP3 and NOCP6.

Figure 9 shows the vertical profiles of the time- and domain-averaged differences (NOCPs minus the STA) of the water
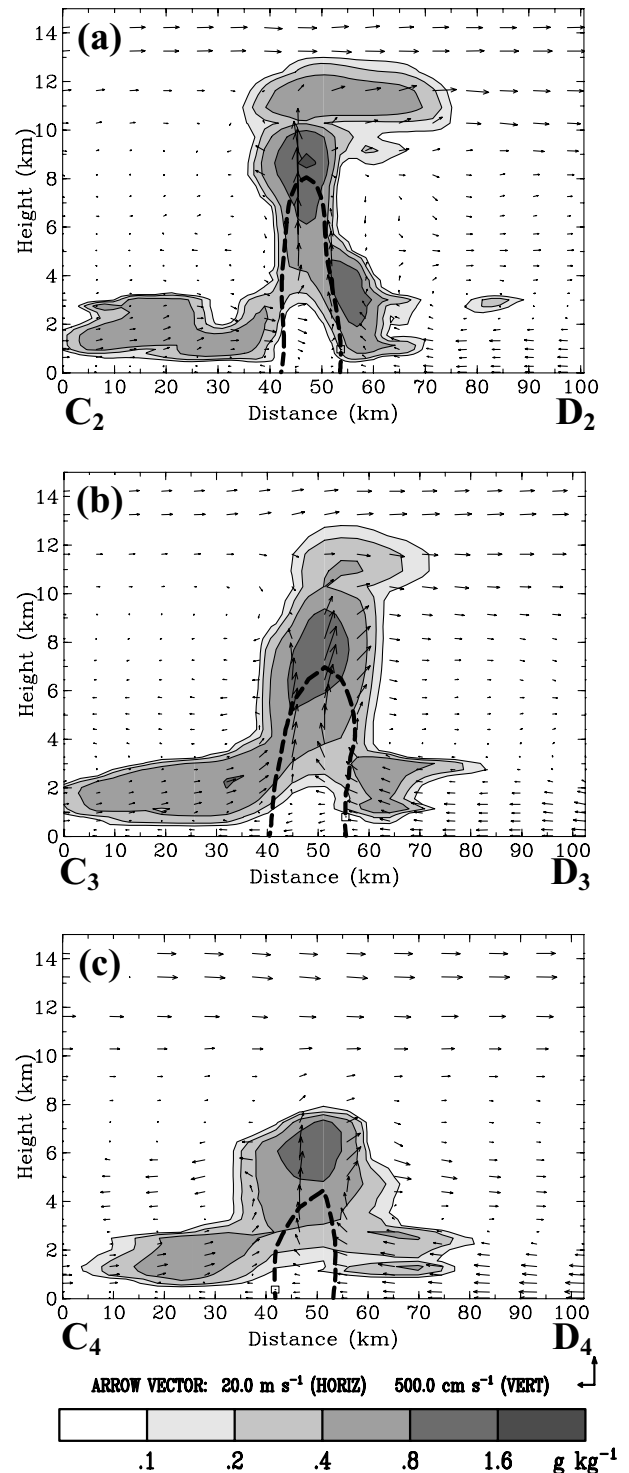

Fig. 7. Same as Fig. 5, but for cross-sections across a mature cell at 1600 UTC 5 August 1998 along the lines (a) 'C$_2$D$_2$' (NOCP3), (b) 'C$_3$D$_3$' (NOCP6) and (c) 'C$_4$D$_4$' (NOCP9) shown in Fig. 6.
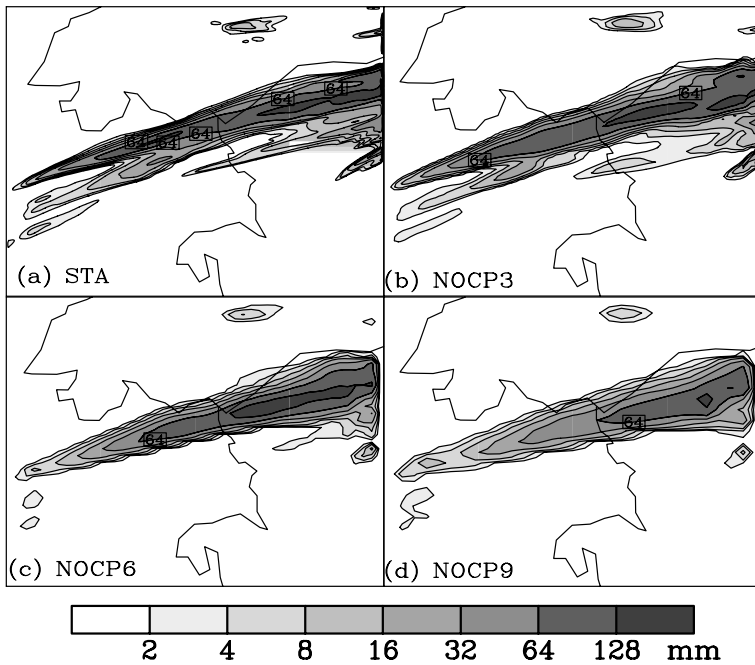
Fig. 8. Horizontal distributions of total rainfall amount for the 6-h period 1200–1800 UTC 5 August 1998 for (a) the STA, (b) NOCP3, (c) NOCP6 and (d) NOCP9. Contour line are 2, 4, 8, 16, 32, 64 and 128 mm.
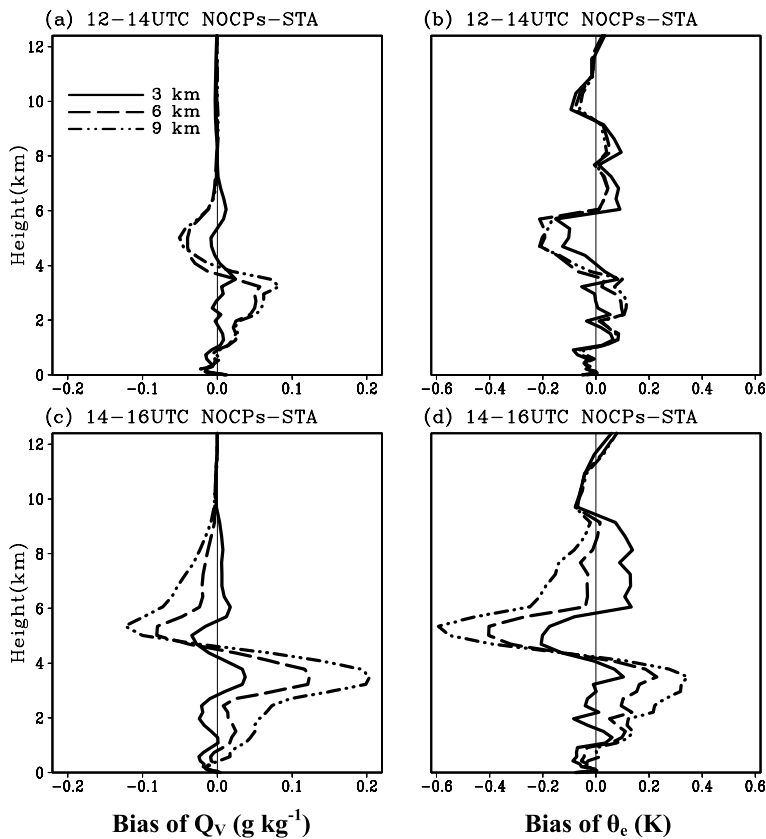

Fig. 9. Profiles of the domain- and time-averaged bias in NOCP simulations (NOCP minus the STA) with different grid spacings (solid: 3 km; dashed: 6 km; dash-double dotted: 9 km): (a, c) water vapour mixing ratio and (b, d) equivalent potential temperature during 1200–1400 UTC (upper panels) and 1400–1600 UTC (lower panels), respectively.

vapour mixing ratio, and the equivalent potential temperature (θ_e). Bias is small for NOCP3 compared to that for NOCP6 and NOCP9. Its magnitudes are significantly larger in the development stage (Figs 9c and d) than those in the formation stage (Figs 9a and b). For the water vapour mixing ratio, couplets of positive (moist) and negative (dry) bias are found in the layer below and above the level of zero bias near the 4.5-km height for 14–16 UTC, respectively. The bias of θ_e reflects both features, showing a maximum positive θ_e bias at about 3 km and a large negative θ_e bias at about 5 km in NOCP6 and NOCP9. As a result, the lower troposphere in NOCPs (especially NOCP9) is more stable than that in the STA. The moisture bias structure in NOCP seems to be associated mainly with the difference in convective development between NOCP and STA. Depth and intensity (i.e. updrafts) of major convective cells along the band decrease with grid size. For example, maximum updraft velocity for 15 UTC is 1.7 m s^{-1} (at 3.5 km) for NOCP9, 5.4 m s^{-1} (at 5.2 km) for NOCP6, 8.5 m s^{-1} (at 6.8 km height) for NOCP3 and 11.1 m s^{-1} (at 8.2 km height) for STA. And cloud development is mainly below about 4.5 km for NOCP9, 6 km for NOCP6 and 10.5 km for NOCP3 and STA (not shown). Thus, convective

transport of low-level moisture to upper levels is much weaker in NOCP9 than that in STA.

NOCPs indicate that a grid resolution of 3 km is sufficient to resolve the convection band considered in this study and convective parameterization may not be necessary. In contrast, a 9-km grid is not sufficient to reproduce the deep convection band. The initial cells that are important for band formation are completely missed. Furthermore, mesoscale circulation associated with the convection band does not develop properly in NOCP9. Simulation with a 6-km grid partly resolves the convection band during its development, but misses the initial cells, similar to NOCP9. Our results also indicate that the bias in atmospheric stability caused by inefficient vertical transport of moisture can be significant for grid sizes of 6 and 9 km.

3.3. Simulations with parameterized convection (KFEXs)

Simulations in this section incorporate parameterized convection using the Kain–Fritsch scheme (Kain and Fritsch, 1990, 1993; Kain, 2004) and are referred to as KFEXs.
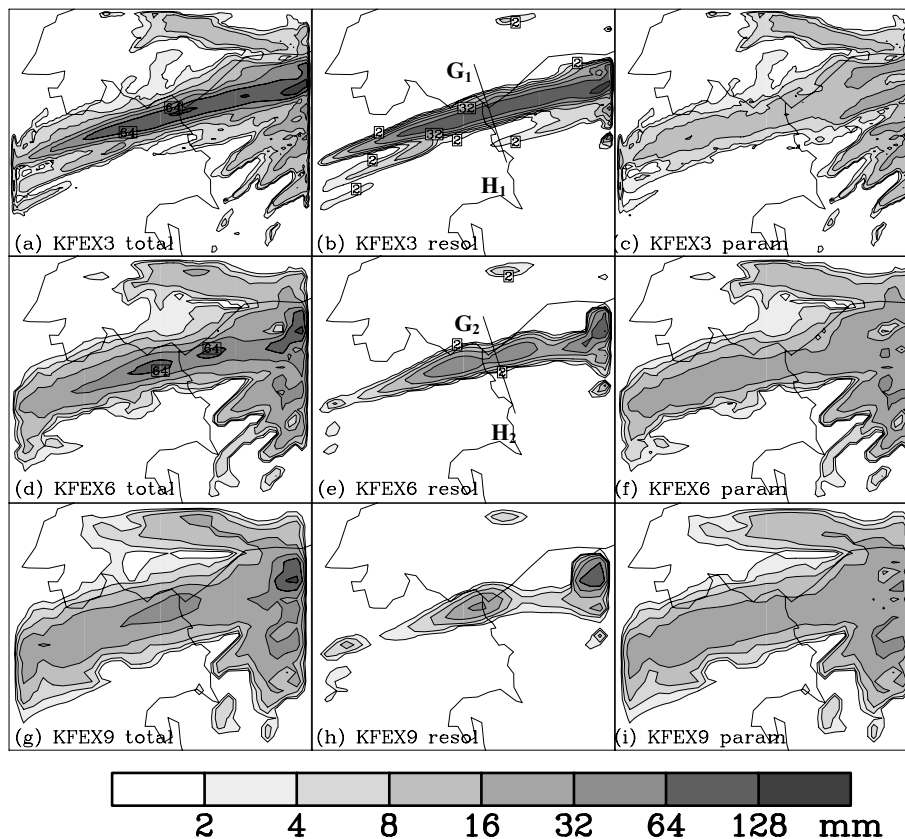

Fig. 10. Horizontal distribution of total (left), grid-resolved (centre) and parameterized (subgrid) (right) rainfall amounts for the 6-h period from 1200 to 1800 UTC 5 August 1998. The upper, middle and lower panels are for KFEX3, KFEX6 and KFEX9, respectively. The lines 'G$_1$H$_1$' and 'G$_2$H$_2$' represent the locations of the cross-sections shown in Fig. 14.

The horizontal distributions of the amount of 6-h rainfall from KFEXs are shown in Fig. 10. The rainfall area is much wider for KFEXs than those for the STA and NOCPs. Furthermore, the total rainfall amount in the major band area decreases rapidly with grid size increasing. The distributions of resolved rainfall (Figs 10b, e and h) in the KFEX simulations match those observed for the STA well in terms of location and width of the band. However, the length of the rain band for a total rainfall amount of greater than 64 mm decreases rapidly with grid size, and is over 200 km in KFEX3 and over 80 km in KFEX6. The maximum amount of rainfall for KFEX9 is no more than 64 mm. The total rainfall amount for the KFEX6 and KFEX9 simulations is dependent mainly on parameterized convection. Furthermore, rainfall in the wide area surrounding the band is largely due to parameterized convection and is incorrectly predicted. It appears that CP is too easily invoked and too much coverage of convective precipitation is predicted.

Comparison of KFEX3 (Fig. 10b) and NOCP3 (Fig. 8b) indicates that the impact of CP is not very significant for the simulation of resolved rainfall band at 3-km grid resolution. The formation and evolution of the resolved band from the two simulations are also very similar to each other according to our examination of resolved fields (not shown). However, the impact increases with grid size. KFEX9 completely misses the development of a resolved convection band, although strong convective systems occur over land at 1800 UTC (not shown).

Figure 11 compares the temporal variation of the precipitation rates averaged over the whole domain for NOCPs and KFEXs. The precipitation rate increases with time as the convection band forms and develops into a mature system. The precipitation rate and its temporal variation for NOCPs are close to those for the STA, except that the rate is underestimated in NOCP9 throughout the period, mainly due to the delayed and weaker convection band (Fig. 11a). The precipitation rate in NOCP6 is underestimated before 1500 UTC, but overestimated after 1600 UTC.

When CP is accounted for in simulations (KFEXs), the total precipitation rate is significantly overestimated in the early stage before 1500 UTC (Fig. 11b). However, it becomes close to the STA after 1500 UTC. Grid-resolved and parameterized precipitation rates are shown in Figs 11c and d, respectively. The resolved precipitation rate of KFEXs is significantly smaller than that for the STA, especially for KFEX6 and KFEX9 (Fig. 11c). The parameterized rate increases with grid size, but does not change much over time (Fig. 11d). As shown in Figs 10f and i, a significant portion of the parameterized rainfall is falsely predicted in the area surrounding the band. Thus, the similarity of the KFEX precipitation rate to the STA rate after 1500 UTC in Fig. 11b is not sufficient to allow prediction of the convection band.

CP tends to produce an excessive drying/moistening in the layer below/above the 4-km height in the band formation stage (12–14 UTC) (Fig. 12). This tendency becomes clearer as grid
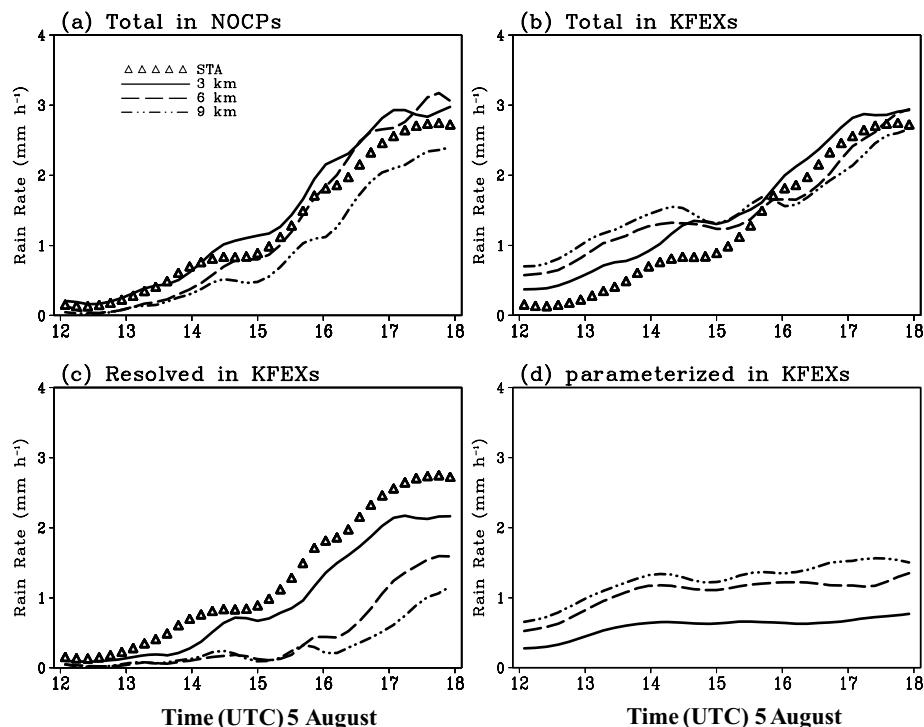

Fig. 11. Temporal variation of domain-averaged rainfall rates for (a) NOCPs and (b–d) KFEXs [(b) total (resolved + subgrid), (c) grid-resolved and (d) sub-grid rainfall rates]. Each line represents an experiment: the STA (triangle) and simulations with 3 km (solid), 6 km (dashed) and 9 km (dash-double dotted) grids.
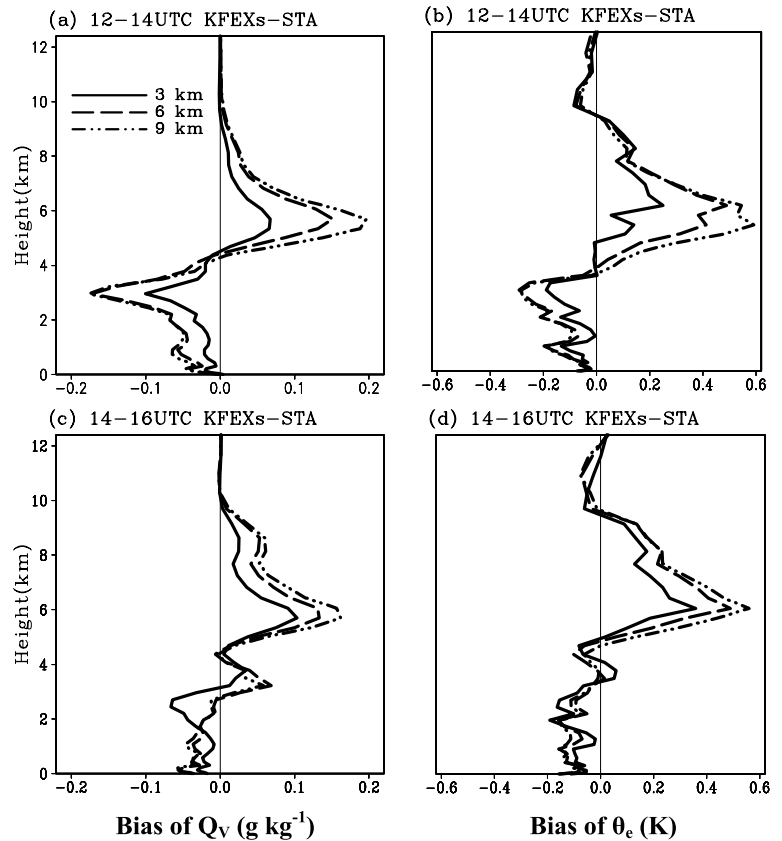
Fig. 12. Same as Fig. 9, but for KFEXs.

Bias of Q_V (g kg^{-1})   **Bias of θ_e (K)**

size increases. Parameterized convection effectively removes instability. However, it removes instability too readily.

Moisture-bias profiles in the simulations with CP are inverted compared to the NOCP results (see Figs 9 and 12). Thus, both simulations with and without CP do not accurately simulate the atmospheric structure surrounding the convection band. For a grid size of 3 km, the two simulations produce results fairly close to the STA fields. For coarser grids (i.e. 6- and 9-km grids), however, the precipitation systems predicted from NOCP6 and NOCP9 are more similar to the STA than those predicted from KFEX6 and KFEX9. Furthermore, simulations with CP result in the forecast of spurious precipitation. If CP is not included in simulations, there may be late development of the precipitation system in the formation stage and ineffective removal of instability. The latter may result in false rainfall predictions in forecasts for longer time periods than the present integration period (9 h). This possibility needs to be investigated further.

4. Simulations with a modified trigger function

As pointed out in the previous section, both simulations with and without CP do not simulate the atmospheric structure surrounding the convection band accurately. In this section, we employ the modified trigger function proposed by Ma and Tan (2009) in the KF scheme to further examine whether CP is useful for

simulations at lower resolutions (i.e. 6- and 9-km grids). The current and modified trigger functions are explained below in brief.

Beginning at the surface, vertically adjacent model layers are mixed until the total depth becomes at least 50 hPa. The thermodynamic properties of this updraft source layer (USL) are mass weighted. The USL is lifted to its lifting condensation level (LCL), where its temperature is T_{LCL}. This lifted air is usually colder than its environment (with temperature T_{ENV}) and is negatively buoyant. A temperature perturbation (ΔT) is added to T_{LCL} to drive the parcel. This temperature perturbation is defined as

$$\Delta T = kW_G^{1/3}, \tag{1}$$

where k is a unit number with dimensions K s$^{1/3}$ cm$^{-1/3}$ and W_G is a function of the grid-scale vertical velocity, the grid spacing and the LCL height of the USL (Fritsch and Chappell, 1980; Kain, 2004). The following criterion is then checked to see if convection should be initiated:

$$\begin{cases} T_{LCL} + \Delta T > T_{ENV}, & \text{convection initiates} \\ \text{otherwise}, & \text{search for next potential USL} \end{cases} \tag{2}$$

The definition of ΔT is crucial in determining whether convection should be triggered. In this study, we found that the current definition triggers parameterized convection

inappropriately. Recently, a new algorithm to define the temperature perturbation was proposed by Ma and Tan (2009):

$$\Delta T = C_{\mathrm{h}}\delta T_{\mathrm{h}} + C_{\mathrm{v}}\delta T_{\mathrm{v}}, \tag{3}$$

where δT_{h} is the spatial anomaly of temperature for each local grid against the horizontal mean of its environmental temperature (i.e. average over nine adjacent grid points surrounding the grid point of interest), δT_{v} the temperature anomaly against the vertical mean temperature (i.e. average over the three sigma levels, LCL-1, LCL and LCL+1). The non-dimensional coefficients C_{h} and C_{v} are the normalized horizontal and vertical moisture advection, respectively. The normalization algorithm is as follows:

$$C_{\mathrm{h,v}} = \frac{\vec{V}\cdot\nabla q - \min(\vec{V}\cdot\nabla q)_{\mathrm{h,v}}}{\max(\vec{V}\cdot\nabla q)_{\mathrm{h,v}} - \min(\vec{V}\cdot\nabla q)_{\mathrm{h,v}}}, \tag{4}$$

where $\max(\vec{V}\cdot\nabla q)_{\mathrm{h,v}}$ and $\min(\vec{V}\cdot\nabla q)_{\mathrm{h,v}}$ are calculated within the same grid boxes as that of δT_{h} and δT_{v}.

By adding a positive relationship between the grid-scale temperature anomaly (represented by the effect of environmental forcing) and local forced convective disturbance, Ma and Tan (2009) demonstrate that the new algorithm reduces subgrid-scale rainfall considerably and removes instability under weak environmental forcing effectively. In this study, we modify the calculation of the vertical average of environment temperature, because the average of temperatures at three vertical grids is not exactly the average value at the mid-grid level in a vertically stretched grid system. Here, using linear interpolation, we first obtain the temperature at the height (within the upper box) whose distance from the mid grid level is the same as the grid depth below the mid-grid level. Then, we perform vertical averaging using the interpolated value and the values for the mid and lower grids. We designate MTEXs for the group of grey-zone experiments using Ma and Tan's (2009) definition of temperature perturbation.

Simulated 6-h precipitation amounts for 1200–1800 UTC from MTEXs are shown in Fig. 13. A narrow band of heavy rain is seen for MTEX3 and MTEX6, similar to the STA (Figs 13a and d). The band is due mainly to resolved rainfall (Figs 13b and e). Parameterized rainfall over the coastal area also shows a band-type distribution, but the amount of rainfall is significantly smaller than the resolved rainfall. The total amount of rainfall along the band is much lower for MTEX9 than for MTEX3 and MTEX6. Comparison of Figs 10 and 13 reveals notable differences between MTEXs and KFEXs. The area of
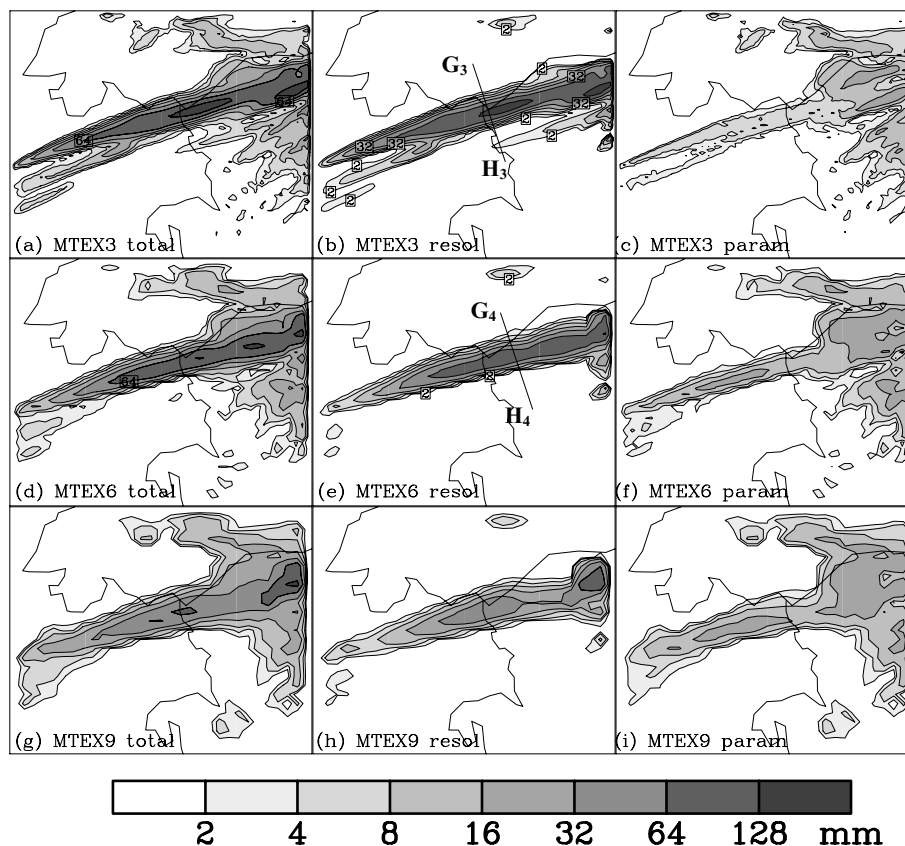

Fig. 13. Same as Fig. 10, but for MTEXs. The lines 'G₃H₃' and 'G₄H₄' represent the locations of the cross-sections shown in Fig. 14.
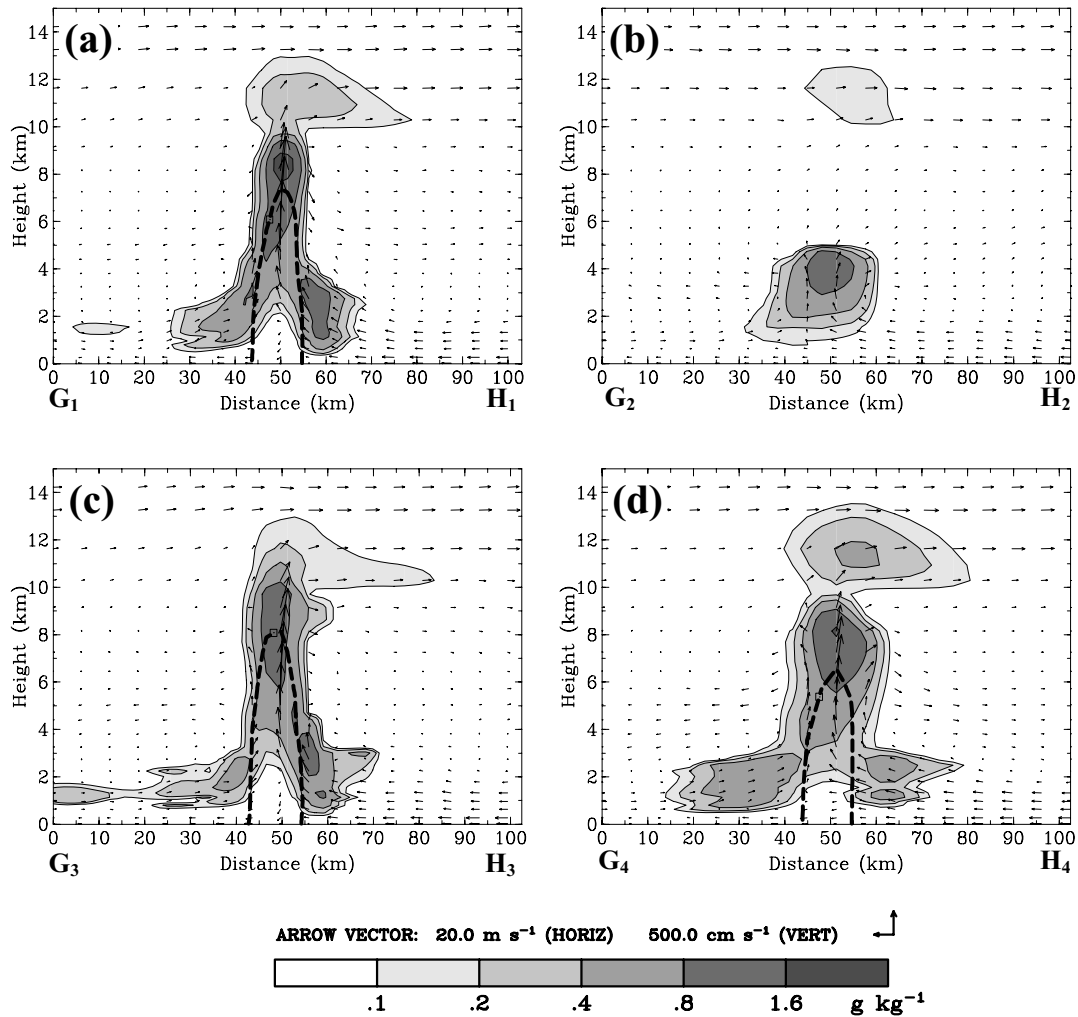
Fig. 14. Same as Fig. 5, but for cross-sections over a resolved mature cell at 1600 UTC 5 August 1998 along the lines (a) 'G$_1$H$_1$' (KFEX3) and (b) 'G$_2$H$_2$' (KFEX6) shown in Fig. 10 and (c) 'G$_3$H$_3$' (MTEX3) and (d) 'G$_4$H$_4$' (MTEX6) shown in Fig. 13.

parameterized rainfall is significantly smaller for MTEXs than for KFEXs, especially in the area surrounding the band. In MTEXs, parameterized convection is triggered mostly along the band, and only rarely in the area of inflow air. This allows stronger development of a resolved convection band.

Vertical cross-sections of the resolved cloud systems at 1600 UTC from KFEXs and MTEXs are shown in Fig. 14. Resolved clouds and circulations for KFEX3 and MTEX3 are similar in size and structure, with two branches of air lifting below 4 km height, strong updrafts of up to about 10 km in height and anvil clouds (Figs 14a and c). However, there are significant differences in shape and structure between KFEX6 and MTEX6 (Figs 14b and d). In KFEX6, resolved deep convection and its associated circulation do not develop. Instead, a shallow convection system is found along the band. In contrast, MTEX6 is still able to reproduce resolved deep convection similar to that produced by MTEX3.

Figure 15 shows the total precipitation rates averaged over the whole domain from the STA, NOCPs, KFEXs and MTEXs. The rates for MTEXs are generally closer to those of the STA than those of KFEXs. Improvement is more noticeable for the 6-km grid simulation (MTEX6). For the 9-km grid, all simulations show significant discrepancies from the STA. Comparison of bias profiles indicates that the bias of MTEX6 is significantly smaller than that of NOCP6 and KFEX6 (Fig. 16). Furthermore, for the 9-km grid simulations, the bias of θ_e for MTEX9 is smaller throughout much of the troposphere than for the other simulations.

The comparisons between the three sets of experiments may be summarized as follows. For the 3-km grid simulations, NOCP simulations produce results for the simulated fields that are more similar to the STA than KFEX and MTEX, although differences between the simulations are not large. The CP experiments reveal that including CP in simulations is not necessary. Use of
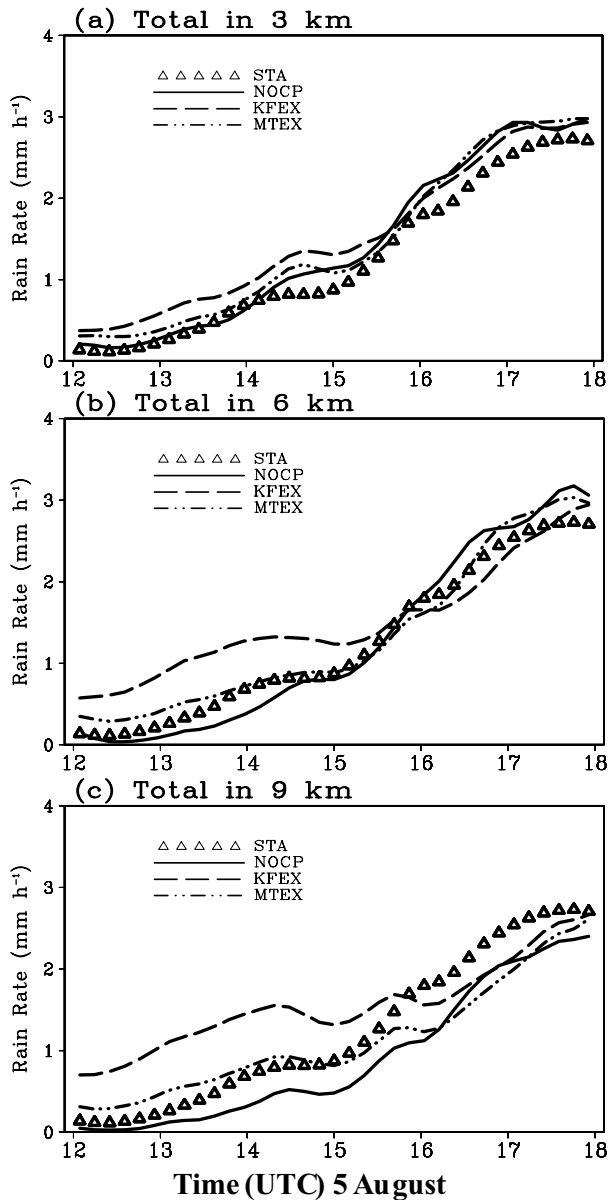
(a) Total in 3 km

(b) Total in 6 km

(c) Total in 9 km

Time (UTC) 5 August

Fig. 15. Temporal variation of the domain-averaged total rainfall rates for simulations with grid sizes of (a) 3 km, (b) 6 km and (c) 9 km. Each line represents an experiment: the STA (triangle), NOCPs (solid), KFEXs (dashed) and MTEXs (dash-double dotted).

the original KF scheme degrades the quality of simulations by producing more rainfall during the early stage of band development and significant bias in the average vertical structure of thermodynamic fields.

For the 6-km grid simulations, both NOCP and MTEX simulations produce comparable results. The NOCP and MTEX simulation results also agree with the STA fairly well. Use of the new temperature perturbation definition of Ma and Tan (2009) for the trigger function in the KF scheme improves the original KF scheme as follows: (1) the area of parameterized convec-

tion is significantly reduced, (2) over-prediction of the domain-averaged rainfall amount in the early stage is significantly reduced, (3) a stronger resolved convection band develops and (4) the bias in the vertical structure of air surrounding the convection band is reduced. In particular, MTEX6 shows a noticeably smaller bias than NOCP6 and KFEX6 throughout much of the troposphere. This suggests that use of the modified trigger function in the KF scheme for simulations of convection bands is a good choice.

For a 9-km grid size, both simulations with and without CP are substantially different from the STA: (1) the total rainfall amount is significantly smaller, (2) the development of resolved convection is weak, especially using the original KF scheme and (3) the bias in the vertical structure of environmental air is significant. Thus, a grid size of 9-km is not sufficient for simulations of the band type convection considered in this study.

5. Conclusions

We have investigated the role of convective parameterization in simulations of a convection band at grey-zone (2–10 km) resolution using OSSE. The case considered for this study is an intensive quasi-stationary convection band that occurred on 5–6 August 1998 over the middle of the Korean Peninsula. The MM5 (Dudhia, 1993; Grell et al., 1994) is used for this study.

This study indicates that 3 km is sufficient to resolve the convection band considered in this study and convective parameterization may not be necessary. In contrast, 9 km is not sufficient to reproduce the deep convection band and parameterized convection tends to suppress the development of resolved convection band.

Both simulations with and without CP are deficient in simulating the atmospheric structure surrounding the convection band. One of the major problems in simulations using CP is excessive triggering of parameterized convection. False triggering of CP in the area surrounding the convection band may weaken or suppress the development of a resolved convection band through excessive stabilization of inflow air. Significant improvement for this problem has been obtained by using the formula of Ma and Tan (2009) for temperature perturbation in the trigger function of the KF scheme. The improvements are more noticeable for the simulations with a 6-km grid, indicating that KF CP with the modification of Ma and Tan (2009) can be useful.

The generality of our conclusions needs to be confirmed, because this study is based on only a convection band event and a numerical model (MM5). Investigations with more cases (e.g. heavy precipitation systems associated with fronts and cloud clusters, etc.) and other NWP models (e.g. WRF) are desirable.
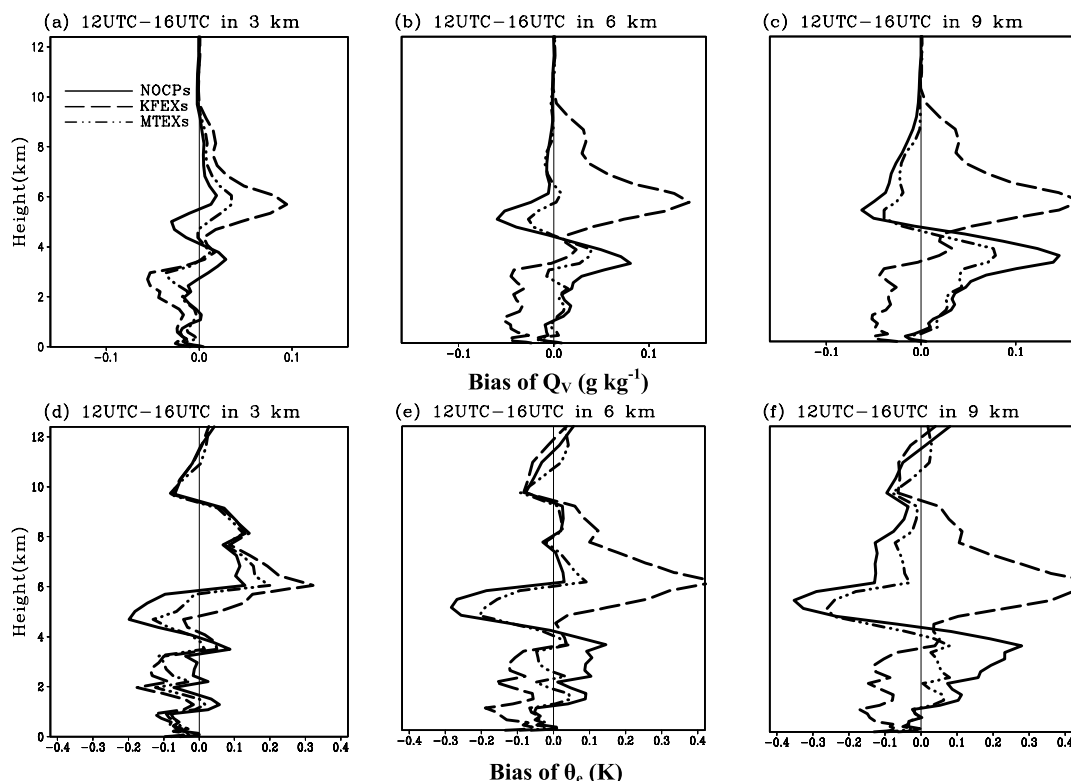
6. Acknowledgments

Fig. 16. Profiles of the domain- and time-averaged bias of Q_v (upper panels) and θ_e (lower panels) in NOCPs (solid), KFEXs (dashed), and MTEXs (dash-double dotted) for grid sizes of (a, d) 3 km, (b, e) 6 km and (c, f) 9 km. Bias is averaged over the whole domain and the period from 1200 to 1600 UTC.

References

Adlerman, E. J. and Droegemeier, K. K. 2002. The sensitivity of numerically simulated cyclic mesocyclogenesis to variations in model physical and computational parameters. *Mon. Wea. Rev.* **130**, 2671–2691.

Arakawa, A. 2004. The cumulus parameterization problem: past, present, and future. *J. Climate* **17**, 2493–2525.

Arakawa, A. and Chen, J. M. 1987. Closure assumptions in the cumulus parameterization problem. In: *Short and Medium Range Numerical Weather Prediction* (ed. T. Matsuno). *Jpn Meteor. Soc.*, 107–131.

Bryan, G. H., Wyngaard, J. C. and Fritsch, J. M. 2003. Resolution requirements for the simulation of deep moist convection. *Mon. Wea. Rev.* **131**, 2394–2416.

Craig, G. C. and Dörnbrack, A. 2008. Entrainment in cumulus clouds: what resolution is cloud-resolving?. *J. Atmos. Sci.* **65**, 3978–3988.

Deng, A. and Stauffer, D. R. 2006. On improving 4-km mesoscale model simulations. *J. Appl. Meteor. Climatol.* **45**, 361–381.

Dudhia, J. 1993. A nonhydrostatic version of the Penn State-NCAR Mesoscale Model: validation tests and simulation of an Atlantic cyclone and cold front. *Mon. Wea. Rev.* **121**, 1493–1513.

Fritsch, J. M. and Chappell, C. F. 1980. Numerical prediction of convectively driven mesoscale pressure systems. Part I: Convective parameterization. *J. Atmos. Sci.* **37**, 1722–1733.

Gerard, L. 2007. An integrated package for subgrid convection, clouds and precipitation compatible with meso-gamma scales. *Quart. J. Roy. Meteor. Soc.* **133**, 711–730.

Gerard, L. and Geleyn, J.-F. 2005. Evolution of a subgrid deep convection parameterization in a limited area model with increasing resolution. *Quart. J. Roy. Meteor. Soc.* **131**, 2293–2312.

Grell, G., Dudhia, J. and Stauffer, D. 1994. A description of the Fifth-Generation Penn State/NCAR Mesoscale Model (MM5). NCAR Technical Note NCAR/TN-398+STR, 138 pp.

Hammarstrand, U. 1998. Questions involving the use of traditional convection parameterization in NWP models with higher resolution. *Tellus* **50A**, 265–282.

Kain, J. S. 2004. The Kain-Fritsch convective parameterization: an update. *J. Appl. Meteor.* **43**, 170–181.

Kain, J. S. and Fritsch, J. M. 1990. A one-dimensional entraining/detraining plume model and its application in convective parameterization. *J. Atmos. Sci.* **47**, 2784–2802.

Kain, J. S. and Fritsch, J. M. 1993. Convective parameterization for mesoscale models: the Kain-Fritsch scheme. In: *The Representation of Cumulus Convection in Numerical Models, Meteor. Monogr.*, No. 46, *Amer. Meteor. Soc.*, 165–170.

Kain, J. S., Weiss, S. J., Bright, D. R., Levit, J. J., Carbin, G. W. and co-authors. 2008. Some practical considerations regarding horizontal

resolution in the first generation of operational convection-allowing NWP. *Wea. Forecasting* **23**, 931–952.

Kalnay, E., Kanamitsu, M., Kistler, R., Collins, W., Deaven, D. and co-authors. 1996. The NCEP/NCAR 40-Year Reanalysis Project. *Bull. Am. Meteor. Soc.* **77**, 437–471.

Kotroni, V. and Lagouvardos, K. 2004. Evaluation of MM5 high-resolution real-time forecasts over the urban area of Athens, Greece. *J. Appl. Meteor.* **43**, 1666–1678.

Kuell, V., Gassmann, A. and Bott, A. 2007. Towards a new hybrid cumulus parameterization schemes for use in non-hydrostatic weather prediction models. *Quart. J. R. Meteor. Soc.* **133**, 479–490.

Lau, K. M., Ding, Y., Wang, J. T., Johnson, R., Keenan, T. and co-authors. 2000. A report of the field operations and early results of the South China Sea Monsoon Experiment (SCSMEX). *Bull. Am. Meteor. Soc.* **81**, 1261–1270.

Lean, H. W., Clark, P. A., Dixon, M., Roberts, N. M., Fitch, A. and co-authors. 2008. Characteristics of high-resolution versions of the Met Office Unified Model for forecasting convection over the United Kingdom. *Mon. Wea. Rev.* **136**, 3408–3424.

Liu, C., Liu, Y. and Xu, H. 2006. A physics-based diffusion scheme for numerical models. *Geophys. Res. Lett.* **33**, doi: 10.1029/2006GL025781.

Ma, L.-M. and Tan, Z.-M. 2009. Improving the behavior of the cumulus parameterization for tropical cyclone prediction: Convection trigger. *Atmos. Res.* **92**, 190–211.

Molinari, J. M. and Dudek, M. 1992. Parameterization of convective precipitation in mesoscale numerical models: a critical review. *Mon. Wea. Rev.* **120**, 326–344.

Niemelä, S. and Fortelius, C. 2005. Applicability of large-scale convection and condensation parameterization to meso-γ-scale HIRLAM: a case study of a convective event. *Mon. Wea. Rev.* **133**, 2422–2435.

Noda, A. and Niino, H. 2003. Critical grid size for simulating convective storms: a case study of the Del City supercell storm. *Geophys. Res. Lett.* **30**, doi: 10.1029/2003GL017498.

Petch, J. C., Brown, A. R. and Gray, M. E. B. 2002. The impact of horizontal resolution on the simulations of convective development over land. *Quart. J. R. Meteor. Soc.* **128**, 2031–2044.

Reisner, J., Rasmussen, R. J. and Bruintjes, R. T. 1998. Explicit forecasting of supercooled liquid water in winter storms using the MM5 Mesoscale Model. *Quart. J. R. Meteor. Soc.* **124B**, 1071–1107.

Roberts, N. M. and Lean, H. W. 2008. Scale-selective verification of rainfall accumulations from high-resolution forecasts of convective events. *Mon. Wea. Rev.* **136**, 78–97.

Saito, K., Ishida, J.-I., Aranami, K., Hara, T., Segawa, T. and co-authors. 2007. Nonhydrostatic atmospheric models and operational development at JMA. *J. Meteor. Soc. Jpn.* **85B**, 271–304.

Schwartz, C. S., Kain, J. S., Weiss, S. J., Xue, M., Bright, D. R. and co-authors. 2009. Next-day convection-allowing WRF model guidance: a second look at 2-km versus 4-km grid spacing. *Mon. Wea. Rev.* **137**, 3351–3372.

Steppeler, J., Hess, R., Schattler, U. and Bonaventura, L. 2003. Review of numerical methods for nonhydrostatic weather prediction models. *Meteorol. Atmos. Phys.* **82**, 287–301.

Sun, J. and Lee, T. Y. 2002. A numerical study of an intensive quasi-stationary convection band over the Korean Peninsula. *J. Meteor. Soc. Jpn.* **80**(5), 1221–1245.

Thompson, G., Rasmussen, R. M. and Manning, K. 2004. Explicit forecasts of winter precipitation using an improved bulk microphysics scheme. Part I: Description and sensitivity analysis. *Mon. Wea. Rev.* **132**, 519–542.

Weisman, M. L., Skamarock, W. C. and Klemp, J. B. 1997. The resolution dependence of explicitly modeled convective systems. *Mon. Wea. Rev.* **125**, 527–548.

Weisman, M. L., Davis, C., Wang, W., Wanning, K. W. and Klemp, J. B. 2008. Experiences with 0–36-h experiments convective forecasts with the WRF-ARW model. *Wea. Forecasting* **23**, 407–437.

Zhang, D.-L. and Anthes, R. A. 1982. A high-resolution model of the planetary boundary layer-sensitivity tests and comparisons with SESAME-79 data. *J. Appl. Meteor.* **21**, 1594–1609.